EDGE ARTICLE

Regulation of heteroatom positioning in multiple resonance thermally activated delayed fluorescence materials: performance optimization for blue/red emission

Lifang Yin,[a] Yi Zhao,[a] Qiang Gao,[a] Yajun Yin,[a] Tengfei He,[a] Yufei Yang,[a] Aimin Ren, [iD][a] Tongshun Wu,[b] Hui Li[a] and Luyi Zou [iD] *[a]

Strategically incorporating Se into B/N-heteropolycyclic frameworks is key to modulating multiple resonance (MR) systems and developing high-performance TADF materials. Combining density functional theory and spin-component scaled coupled cluster calculations, this study reveals the TADF mechanism regulated by the heavy-atom effect in model molecule **BNSSe**, and designs two types of high-performance MR-TADF materials based on **BNSSe**. (1) The blue-emission molecule **1** (469 nm) achieves complementary short-range charge transfer/long-range charge transfer advantages via three $para$-B−π−N units. Its reverse intersystem crossing rate (k_{RISC}) reaches 10^8 s^{-1} (three orders of magnitude higher than **BNSSe**), benefiting from the synergy of a reduced singlet−triplet energy gap, moderately enhanced spin−orbit coupling (SOC), and suppressed structural relaxation. (2) The red-emission molecules **2−7** ($\approx$630 nm) were further developed via a delicately designed π-bonding/non-bonding molecular orbital hybridization strategy. This series of molecules not only maintain a high radiative decay rate but also effectively inhibit the non-radiative decay process, and their design concept is expected to break through the constraints of the traditional energy gap law. Theoretical studies reveal that the spatial position of heteroatoms can modulate molecular geometry and induce axial redistribution of frontier molecular orbital electron density, thereby selectively enhancing the contribution of Se atoms to the excited-state transition orbitals and enabling precise regulation of SOC strength. This work not only deepens the theoretical understanding of the heavy-atom effect mechanism but also provides a new strategy for developing high-performance MR-TADF materials through the targeted regulation of SOC and k_{RISC} via atomic site engineering.

1 Introduction

Organic light-emitting diodes (OLEDs), as the core of next-generation display technologies, have achieved a leapfrog upgrade from traditional display devices to intelligent interface platforms integrating three features: functional integration, diverse forms, and scenario adaptation.[1] Their breakthroughs in high contrast, flexible integration, and low latency will continue to redefine future human–computer interaction modes. The key to the breakthrough of this technology lies in the iterative innovation of materials. Thermally activated delayed fluorescence (TADF) materials, with the dual advantages of 100% exciton utilization and no noble metal dependence, are widely recognized in the industry as the most promising next-generation luminescent materials after phosphorescent materials.[2–5]

In recent years, multiple resonance (MR)-TADF materials have shown narrow emission bands (full width at half maximum, FWHM < 70 nm). This is attributed to their rigid structural skeletons and localized distribution of frontier molecular orbitals (FMOs), which result in weak electron-vibration coupling and small structural relaxation. They have thus become a key material system for achieving the BT.2020 ultra-high-definition display color gamut standard.[6–13] However, such materials still face severe challenges in practical device applications. Limited by relatively low reverse intersystem crossing rates (k_{RISC}, usually <10^5 s^{-1}), triplet excitons accumulate excessively at high current densities. This is because they cannot be rapidly converted to singlet excitons through the RISC channel. Such accumulation leads to significant efficiency roll-off via non-radiative pathways like triplet–triplet annihilation.[14,15] This phenomenon is particularly prominent in blue-emitting MR-TADF materials. Their high triplet energy levels

[a]Institute of Theoretical Chemistry, College of Chemistry, Jilin University, Changchun 130023, P. R. China. E-mail: zouly@jlu.edu.cn

[b]Key Laboratory of Functional Materials Physics and Chemistry of Ministry of Education, Jilin Normal University, Changchun 130103, China

(T_1 > 2.8 eV) not only exacerbate exciton annihilation effects but also easily trigger radical cation degradation (*e.g.*, intramolecular cyclization reactions). As a result, the device lifetime (LT50) is generally less than 100 hours.[16]

For molecular design aiming to enhance k_{RISC}, there are currently two main strategies. One is to reduce the singlet–triplet energy gap (ΔE_{ST}) by expanding the B/N skeleton. For example, Huang *et al.* developed DABNA-3B and BCzBN-3B blue-emitting materials based on the π-extension strategy of B–N covalent bonds, with their k_{RISC} reaching 10^5 s^{-1}.[17] Although this performance is outstanding among pure organic MR-TADF materials, it still lags behind that of typical metal complex systems (>10^6 s^{-1}). The other is to enhance the spin–orbit coupling (SOC) effect by introducing heavy atoms. For instance, the BNSSe and BNSeSe green-emitting materials designed by Hu *et al.* achieved a k_{RISC} of 10^5–10^6 s^{-1} through embedding Se atoms into the B/N skeleton.[18] In particular, the Yasuda group from Kyushu University achieved a k_{RISC} of 10^8 s^{-1} in the CzBSe molecule by introducing Se atoms.[19] These findings provide important insights for the molecular design in this study. By synergistically regulating B/N skeleton expansion and heavy atom effects, it is expected that the existing k_{RISC} limit will be broken.

Inspired by the above strategies, two key scientific questions are proposed from the perspective of synergizing excited-state regulation and molecular engineering. First, how can precise π-extension of the B/N skeleton be achieved through structural design while maintaining the MR effect? This process requires establishing a dynamic balance mechanism of "orbital localization–delocalization". Excessive delocalization weakens the atomic localization of frontier molecular orbitals, leading to intensified vibrational relaxation. Insufficient extension, however, fails to effectively reduce ΔE_{ST} to enhance k_{RISC}. Second, although introducing Se atoms can significantly improve k_{RISC}, the synthesis of organic Se compounds often faces great challenges. In practical applications, it is necessary to balance the amount of Se atoms introduced and performance gains. Then, how can the two be balanced to maximize k_{RISC} while keeping the number of Se atoms unchanged? By cleverly designing the molecular geometry and electronic distribution, it may be possible to effectively regulate the excited-state properties. This can give full play to the advantages of the heavy atom effect while minimizing the amount of Se atoms introduced. The potential of Se atom introduction in improving k_{RISC} performance is further explored, providing new ideas for the design and development of related materials.

Current systematic investigations of MR-TADF materials in our group reveal a pronounced imbalance in development among the three primary colors (red, green, blue).[20] Compared to the significant advancements in blue and green systems, research progress on pure red MR-TADF emitters substantially lags behind, as evidenced by both the scarcity of reported molecular structures and their inferior photophysical performances. The reasons include, in addition to solving common issues such as k_{RISC} enhancement, that red emitters face special challenges from the energy gap law. That is, as the emission wavelength redshifts, the reduced energy gap leads to

a significant increase in non-radiative transition rates, resulting in a sharp decline in luminous efficiency. This creates a dilemma where high luminous efficiency and red emission are difficult to reconcile, severely restricting the commercial development of OLED display technology.[21,22] Although Liu *et al.* achieved a redshift of the emission spectrum by introducing strong electron-withdrawing cyano groups to lower the lowest unoccupied molecular orbital (LUMO) energy level, and developed CNCz–BNCz as the first orange-red MR-TADF material, its emission peak at 581 nm still has a significant gap from the 630 nm red emitter required by the BT.2020 standard.[23,24] This performance gap severely hinders the commercialization of OLED full-color display technology, highlighting the urgency of theoretical innovation and molecular design breakthroughs in the development of red material systems.

Based on the **BNSSe** molecular skeleton containing a single Se atom, we introduced a B/N fused-ring rigid structure for π-extension and synergistically utilized the heavy atom effect, designing molecule **1** with fast RISC characteristics (Fig. 1). Compared with the molecule **BNSSe** with short-range charge transfer (SRCT) properties, molecule **1** exhibits hybrid SRCT/long-range CT (LRCT) characteristics due to the expanded B/N skeleton. It has both a smaller ΔE_{ST} and a larger SOC, increasing the k_{RISC} to 10^8 s^{-1} (a 3-orders-of-magnitude enhancement), which is comparable to that of typical metal complex systems. Meanwhile, molecule **1** adopts a modification strategy using three sets of *para*-B–π–N units, which synergistically weakens the electron-withdrawing/donating abilities of B/N atoms. This raises the LUMO energy level and lowers the HOMO energy level, significantly widening the HOMO–LUMO energy gap (ΔE_{H-L}) and achieving a blue-shifted emission wavelength of 469 nm. This result provides a new design idea for developing blue TADF materials with both high k_{RISC} and narrowband emission.

To meet the BT.2020 standard requirements for pure red emitters, we modified the skeleton of molecule **1**. By exchanging N and B atoms at specific sites, we constructed molecule **1-a** containing two sets of *para*-N–π–N and one set of *para*-B–π–B structures. This design significantly enhanced the electron-withdrawing/donating abilities of B/N atoms, increasing the HOMO energy level and lowering the LUMO energy level. The ΔE_{H-L} was notably reduced. Combined with the π-conjugation extension effect of the rigid fused ring, its emission spectrum redshifted to 703 nm. However, this wavelength deviates from the target value. Further studies revealed that although molecule **1-a** exhibits certain SRCT characteristics, the two lower N atoms are directly bonded to the benzene rings at both ends. While this structure enhances molecular rigidity, excessive conjugation causes electron clouds to be overly localized in the π bonding orbitals of the three central benzene rings. As a result, the reorganization energy is only slightly lower than that of the **BNSSe** molecule. Combined with the ultra-narrow energy gap effect, the non-radiative transition rate (k_{nr}^S = 4.18 × 10^7 s^{-1}) significantly exceeds the radiative transition rate (k_r^S = 1.81 × 10^7 s^{-1}), leading to luminescence quenching. Drawing on these results, we adjusted the design strategy. While keeping the main skeleton unchanged, we
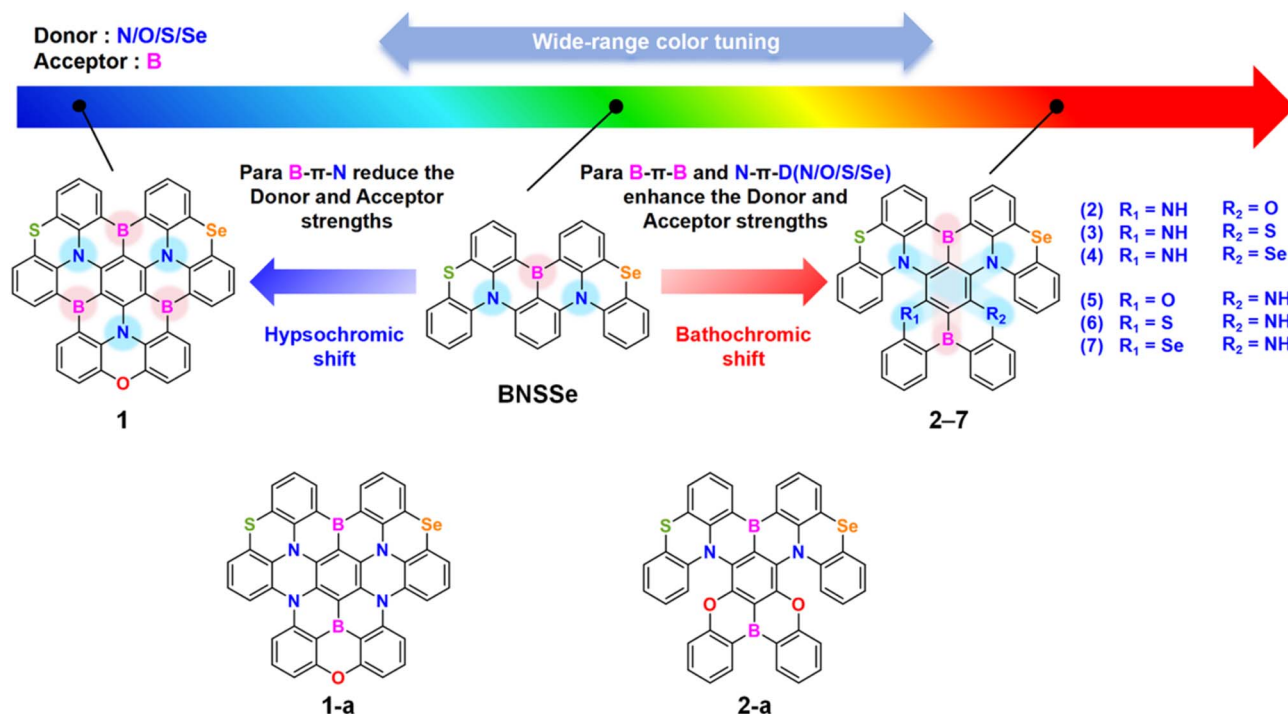
Fig. 1 Schematic of the investigated molecular structures.

innovatively fused the DOBNA[25] molecule (with significant MR-TADF characteristics) with the **BNSSe** skeleton to construct molecule **2-a**. This design introduced an O-bridged unit to break the direct connection between the two lower N atoms and the benzene rings at both ends, forming a unique B–N–O structural arrangement. This structure not only enhances SRCT characteristics but also, through the hybrid π-bonding/non-bonding molecular orbitals formed by the central benzene ring with B, N, and O units, effectively reduces the reorganization energy while maintaining the same order of magnitude of radiative transition rate as molecule **1-a**. Thus, the non-radiative transition rate is significantly reduced ($k_{nr}^S = 2.48 \times 10^5$ s^{-1}). However, the emission wavelength of molecule **2-a** is 595 nm, still deviating from the target of 630 nm (Fig. S8–S10 and Table S8). To further optimize performance, we attempted fine regulation. By replacing one O atom with an N atom (with stronger electron-donating ability), we designed molecules **2** and **5**, whose emission wavelengths were successfully adjusted to around 630 nm. Subsequently, based on molecules **2** and **5**, we introduced S and Se atoms (with heavy atom effects) to replace O atoms, constructing molecules **3/6** and **4/7**, respectively. All these molecules achieved pure red emission around 630 nm. Meanwhile, their k_{nr}^S is much smaller than k_r^S, creating conditions to break through the limitations of the energy gap law.

Notably, given the asymmetric structural characteristics of the parent molecule **BNSSe**, in our designed red emitters **2–7**, with the main skeleton unchanged, only adjusting the relative positions of the lower heteroatoms (O/S/Se) and Se in the main skeleton for the two structures of B–π–B/Se–N–π–N (R$_1$= = NH, R$_2$= = O/S/Se) and B–π–B/S–N–π–N (R$_1$= = O/S/Se, R$_2$= = NH) can cause a certain degree of change in geometric structure.

This further drives the rearrangement of FMO axial distribution. With the rearrangement of FMO axial distribution, the contribution of Se atoms in the main skeleton to excited-state transition orbitals is directionally regulated, ultimately leading to significant differences in SOC and RISC rates. This core finding challenges the cognitive framework of traditional heavy atom effects: the enhancement of SOC not only depends on the number of Se heavy atoms. When the number of Se atoms is the same, differences in the spatial sites of heteroatoms can indirectly regulate the contribution of Se atoms to excited-state transition orbitals, thus giving fuller play to the advantages of Se's heavy atom effect. This provides important theoretical guidance for in-depth understanding of the intrinsic mechanisms underlying SOC enhancement and RISC rate improvement.

2 Computational methods

2.1 Computational details

Choosing appropriate theoretical methods is the cornerstone for accurately simulating molecular structures and predicting properties. In this study, for the geometric structures of the ground state (S$_0$), first excited singlet state (S$_1$), and first excited triplet state (T$_1$) of the studied molecules, we optimized them using density functional theory (DFT) and time-dependent DFT (TD-DFT) methods[26–29] *via* the Gaussian 16 program.[30] Meanwhile, the vibrational frequencies of the corresponding structures were calculated to ensure the optimized structures are stable without imaginary frequencies. In both DFT and TD-DFT calculations, the hybrid B3LYP-D3(BJ) functional[31–33] was adopted. For Se atoms, the SDD pseudopotential basis set[34] was

used, while for other atoms, the 6-31G(d) basis set[35] was employed.

Due to the problem that the TD-DFT method severely underestimates the T_1 state energy, the singlet–triplet energy gap (ΔE_{ST}) obtained at the B3LYP-D3(BJ)/6-31G(d) level shows a large deviation from the experimental value (Table S1). Additionally, theoretical studies on MR-TADF molecules have indicated that the TD-DFT method tends to overestimate ΔE_{ST} when simulating MR-TADF molecules, with a mean average deviation (MAD) generally exceeding 0.2 eV. In contrast, the wavefunction-based high-precision spin-component scaling second-order approximate coupled-cluster (SCS-CC2) method[36,37] exhibits higher accuracy, with a MAD of only 0.04 eV.[38] To balance the accuracy of ΔE_{ST} and affordable computational cost, this study combined the TD-B3LYP method and SCS-CC2 method to simulate ΔE_{ST} of all studied MR-TADF molecules. Specifically, based on the S_1 structure optimized at the B3LYP-D3(BJ)/6-31G(d) level, the vertical excitation energies of $S_1 \rightarrow S_0$ and $T_1 \rightarrow S_0$ transitions were calculated using the SCS-CC2 method with the cc-PVTZ basis set via the MRCC program.[39,40]

The spin–orbit coupling (SOC) between singlet and triplet states was calculated using the ORCA 5.0 program[41] based on the S_1 and T_1 state structures optimized by the Gaussian 16 program. The calculations were performed under the one-component zeroth-order regular approximation (ZORA)[42,43] with all atoms uniformly using the B3LYP-D3(BJ)/ZORA-def2-SVP[44] level. The reorganization energy was obtained from calculations using the MOMAP program.[45]

2.2 Radiative and non-radiative decay rate constants

The luminescence mechanism of the studied MR-TADF molecules involves several key processes. These specifically include the prompt fluorescence radiative and non-radiative transition processes of $S_1 \rightarrow S_0$, the phosphorescence radiative and non-radiative processes of $T_1 \rightarrow S_0$, and the intersystem crossing (ISC) and reverse intersystem crossing (RISC) processes between the S_1 and T_1 states.[46]

The prompt fluorescence and phosphorescence transitions can be calculated from Einstein's spontaneous radiation equation.[47]

$$k_r^{S(T)} = \frac{2\pi v^2 e^2}{\varepsilon_0 mc^3} f_{S_1 \rightarrow S_0(T_1 \rightarrow S_0)} \quad (1)$$

where v represents the excitation energy (in units of cm^{-1}) and e signifies the elementary charge. The term ε_0 denotes the vacuum permittivity, m stands for the mass of the electron, c represents the speed of light, and f represents the transition oscillator strength of the $S_1 \rightarrow S_0$ ($T_1 \rightarrow S_0$) transition.

The ISC and RISC rates were calculated according to the formulae proposed by Katsuyuki Shizu and Hironori Kaji.[48] Previously, this method was successfully applied to **BNSSe** series molecules (BNOO, BNSS, and BNSeSe), verifying its accuracy.

$$k_{ISC}(S_1 \rightarrow T_1) = \frac{2\pi}{\hbar}|SOC(S_1 - T_1)|^2 \times LSF_{ISC}(E(S_1) - E(T_1)) \quad (2)$$

$$LSF_{ISC}(E(S_1) - E(T_1)) = \frac{1}{\pi} \frac{\gamma}{\{E(S_1) - E(T_1)\}^2 + \gamma^2} \quad (3)$$

$$k_{RISC}(T_1 \rightarrow S_1) = \frac{1}{3} \times k_{ISC}(S_1 \rightarrow T_1)\exp\left[-\frac{\{E(S_1) - E(T_1)\}}{k_B T}\right] \quad (4)$$

where $|SOC(S_1–T_1)|$ denotes the spin–orbit coupling matrix element (SOCME) between the S_1 and T_1 states, k_B is the Boltzmann constant, T represents temperature, and γ represents the half width at half maximum of the line-shape function (LSF$_{ISC}$). We used FWHM = 1000 cm^{-1} ($\gamma = 500$ cm^{-1}) according to the previous report.[49]

To maintain theoretical consistency with the calculation of ISC/RISC rates, the non-radiative transition rate of $T_1 \rightarrow S_0$ was also calculated using the formula proposed by Katsuyuki Shizu and Hironori Kaji.[48]

$$k_{nr}(T_1 \rightarrow S_0) = \frac{2\pi}{\hbar}|SOC(T_1 - S_0)|^2 \times \frac{1}{3S}LSF_{ISC}(E(T_1) - E(S_0)) \quad (5)$$

where $|SOC(T_1–S_0)|$ denotes the SOCME between the T_1 and S_0 states, and S is an empirical parameter (=2.1947 × 10^5).

The non-radiative transition rate of $S_1 \rightarrow S_0$ was calculated using the MOMAP program.[50] We have also simulated the non-radiative transition rate of the experimental molecule **BNSSe** in the solid-state environment, with specific details provided in the SI (see SI pages 12 and 13).

It should be noted that in the rate calculations, the energies of all singlet and triplet states adopted the values corrected by the SCS-CC2 method.

In addition, we also calculated the quantum efficiency of delayed fluorescence at room temperature.[51]

$$\Phi_{TADF} = \sum_{m=1}^{\infty} (\Phi_{ISC}\Phi_{RISC})^m \Phi_p \quad (6)$$

where Φ_{ISC}, Φ_{RISC}, and Φ_p represent the quantum efficiencies of ISC, RISC, and prompt fluorescence, respectively.

$$\Phi_{ISC} = \frac{k_{ISC}}{k_r^S + k_{IC} + k_{ISC}} \quad (7)$$

$$\Phi_{RISC} = \frac{k_{RISC}}{k_r^T + k_{ISC} + k_{RISC}} \quad (8)$$

$$\Phi_p = \frac{k_r^S}{k_r^S + k_{IC} + k_{ISC}} \quad (9)$$

3 Results and discussion

3.1 Geometry and electronic structure

Geometric differences between the ground and excited states are a key factor determining the photophysical properties of TADF molecules. Superposition analysis of the optimized configurations of the S_0, S_1, and T_1 states of molecules was performed using PyMOL software. The degree of structural

change was quantitatively evaluated using root-mean-square deviation (RMSD,

$$\text{RMSD} = \sqrt{\frac{1}{N}\sum_i [(x_i - x_i')^2 + (y_i - y_i')^2 + (z_i - z_i')^2]}).$$

RMSD analysis (Fig. 2) shows that compared with the parent molecule **BNSSe** (0.098), the structural distortion between the S_0/S_1 states of molecules **1**, **2**, and **5** is reduced. In particular, the RMSD value of molecule **1** is significantly reduced (0.033), indicating that introducing a B/N-containing fused-ring rigid structure (including O atoms with a radius close to that of N atoms) can effectively suppress structural relaxation between the S_0/S_1 states. This enhanced structural rigidity not only facilitates the realization of narrowband emission but also improves the photoluminescence quantum yield (PLQY) by significantly suppressing vibrational coupling losses in non-radiative channels. Although the larger atomic radii of S and Se atoms slightly increase the structural differences between the S_0/S_1 states of molecules **3/6** and **4/7** compared with **BNSSe**, the RMSD values between isomers are highly similar. Does this imply that their photophysical processes are also similar?

In the designed series of red emitters **2–7**, all molecules exhibit small structural differences between the S_1/T_1 states. This structural similarity between excited states is significantly better than the corresponding configurational changes between the S_0/S_1 or S_0/T_1 states, providing a favorable structural basis for efficient ISC and RISC processes. However, bis-Se-containing

molecules **4** and **7** exhibit large configurational differences between the S_0/T_1 states (RMSD = 0.198 and 0.219, respectively). This geometric change may significantly increase the non-radiative transition rate of $T_1 \rightarrow S_0$ by enhancing the nonadiabatic coupling effect. In this case, to maintain efficient TADF properties, a faster k_{RISC} is necessary to enable molecules to smoothly upconvert from the T_1 state to the S_1 state, thereby competitively suppressing triplet quenching channels. We will discuss how to optimize the RISC process through heavy atom effects and molecular orbital regulation in the subsequent rate calculation section.

Frontier molecular orbital (FMO) analysis is a key means to reveal the structure–activity relationship between molecular electronic structures and photophysical properties. The HOMO–LUMO energy gap (ΔE_{H-L}) directly affects the emission color of materials, while its spatial distribution characteristics influence charge transfer properties and emission efficiency. In molecular design, N atoms can significantly raise the HOMO energy level due to the electron-donating nature of their lone pairs. In contrast, B atoms, with the strong electron-withdrawing ability of their empty p orbitals, obviously lower the LUMO energy level. Molecule **1** introduces an additional B–N pair below the parent structure, forming three sets of *para*-B–π–N structures. This design subtly weakens the electron-withdrawing/donating effects of B/N atoms, leading to a lower HOMO energy level and a higher LUMO energy level.
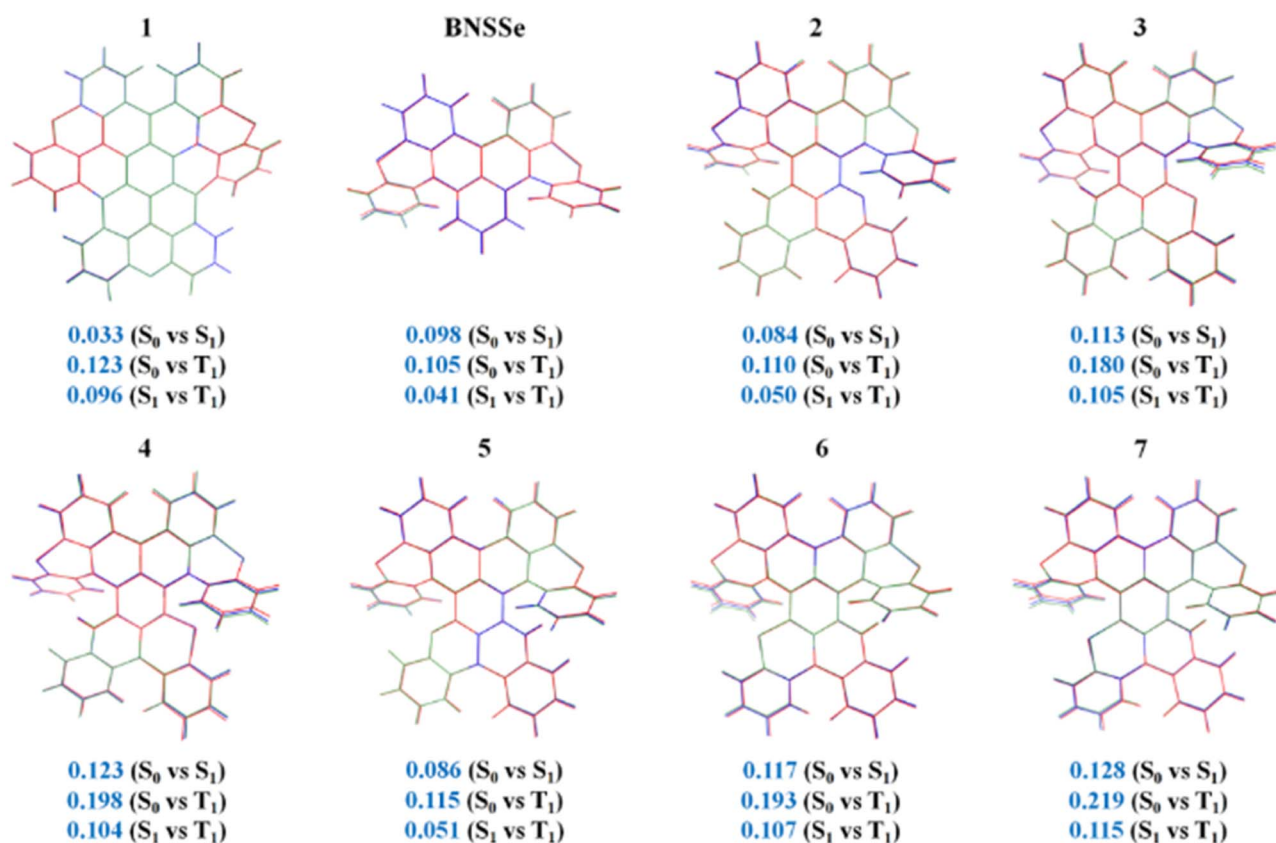

Fig. 2 Superimposed geometric structures of the investigated molecules in S_0 (red), S_1 (blue), and T_1 (green) states with corresponding RMSD (Å) values.

Consequently, $\Delta E_{H–L}$ increases ($\Delta E_{H–L}$ in the S_0 state rises from 3.328 eV to 3.351 eV; $\Delta E_{H–L}$ in the S_1 state increases from 2.981 eV to 3.175 eV), successfully achieving a significant blue shift in absorption/emission spectra. In comparison, molecules **2–7** adopt the *para* structure of B–π–B and N–π–D (donor D = N/O/S/Se). This arrangement synergistically enhances the electron-withdrawing/donating effects of B/D atoms, increasing the HOMO energy level and lowering the LUMO energy level ($\Delta E_{H–L}$ in the S_0 state decreases to 2.633–2.656 eV; $\Delta E_{H–L}$ in the S_1 state reduces to 2.409–2.436 eV), corresponding to a redshift in absorption/emission wavelengths.

Systematic studies on the FMO distribution of molecules in the S_0 and S_1 states (Fig. 3 and S1) reveal the following. For the parent molecule **BNSSe**, the HOMO is mainly localized on electron-donating N/S/Se atoms and adjacent benzene ring C atoms, while the LUMO is primarily concentrated on electron-withdrawing B atoms and surrounding benzene ring C atoms. This distinct SRCT characteristic can effectively suppress electron-vibration coupling, serving as a key structural feature for achieving narrowband emission. For the designed red emitters **2–7**, their HOMO/LUMO distributions are also localized on electron-donating/electron-withdrawing atoms and surrounding benzene rings, maintaining the SRCT characteristic. This allows regulation of spectral redshift while avoiding increased electron-vibration coupling and structural relaxation. As for the designed blue emitter **1**, although the LUMO is mainly localized on atoms, the HOMO is partially localized on the main skeleton atoms and partially delocalized in the lower π-extended region, forming a hybrid SRCT/LRCT characteristic. This dynamic balance mechanism of "orbital localization–delocalization" not only helps reduce ΔE_{ST} but also further improves emission efficiency.

We first conducted a preliminary evaluation of ΔE_{ST}, which is jointly determined by the spatial distance between the HOMO and LUMO ($D_{H–L}$) and the orbital overlap degree ($S_{H–L}$). The energies of S_1 and T_1 are determined by the orbital energy (E) of two unpaired electrons, coulomb repulsion energy (K), and electron exchange energy (J), with specific expressions as follows:

$$E_{S_1} = E + K + J \tag{10}$$

$$E_{T_1} = E + K - J \tag{11}$$

$$\Delta E_{ST} = 2J \tag{12}$$

where J depends on the overlap integral of HOMO and LUMO orbitals ($\int \phi_H \phi_L dr$) and their spatial distance $|r_1 - r_2|$:

$$J = \iint \phi_H(r_1)\phi_L(r_2)\frac{1}{|r_1 - r_2|}\phi_H(r_2)\phi_L(r_1)dr_1dr_2 \tag{13}$$

Here, ϕ_H and ϕ_L are the wavefunctions of HOMO and LUMO orbitals, respectively. The value of ΔE_{ST} can be effectively reduced by decreasing $S_{H–L}$ or increasing $D_{H–L}$. However, different charge transfer characteristics have significantly different impacts on molecular properties. SRCT can effectively suppress electron-vibration coupling and structural relaxation

but often results in larger ΔE_{ST} and slower k_{RISC}. In contrast, LRCT helps reduce ΔE_{ST} by increasing $S_{H–L}$ and shortening $D_{H–L}$ but may exacerbate structural relaxation.[9,10,52,53] Therefore, in molecular design, it is necessary to balance the proportion of SRCT and LRCT as required.

Compared with **BNSSe**, the designed blue emitter **1** shows enhanced intramolecular charge transfer characteristics. This significantly increases $D_{H–L}$ to 3.1329 Å and reduces $S_{H–L}$ to 0.0005 a.u., leading to a notable decrease in the ΔE_{ST} to 0.03 eV, which indicates a significant improvement in RISC rate. Notably, the introduction of the B/N fused-ring structure exhibits multiple synergistic effects. RMSD analysis confirms that this structure can significantly enhance the rigidity of the molecular skeleton, thereby effectively suppressing structural relaxation between S_0/S_1 states. In addition, while imparting LRCT characteristics, this design achieves a synergy between SRCT and LRCT, successfully avoiding non-radiative energy loss pathways caused by electron-vibration coupling and structural relaxation. This strategy of balancing SRCT and LRCT provides a new idea for developing efficient narrow-spectrum luminescent materials.

For the designed red emitters **2–7**, RMSD analysis has shown that replacing O atoms with S/Se (with larger atomic radii) increases the structural differences between S_0/S_1 states. However, by regulating the increase in $S_{H–L}$ and the decrease in $D_{H–L}$, the molecules exhibit stronger SRCT characteristics, still enabling effective suppression of electron-vibration coupling. Although this design moderately increases ΔE_{ST} to approximately 0.2 eV, it is still lower than the energy gap threshold of typical TADF materials (usually <0.3 eV). This ensures that the T_1 state can be upconverted to the S_1 state through thermal activation, achieving TADF emission characteristics. This will provide a reference for the design of red-emitting TADF materials. It is worth noting that although molecules **2–4** and **5–7** all adopt the structural arrangement of *para*-B–π–B and N–π–D (donor D = N/O/S/Se), differences in the positions of heteroatoms O/S/Se lead to significant differences in geometric and electronic structures, which may further result in variations in their photophysical properties.

To address this issue, we conducted an in-depth analysis of the geometric and electronic structures of the S_1 state of molecules **2–7**. According to the Valence Shell Electron Pair Repulsion (VSEPR) theory,[54] electron pairs (including bonding pairs and lone pairs) around the central atom repel each other. They tend to stay as far apart as possible in space, thus determining the molecular geometry. Within this theoretical framework, the observed structural differences can be described more accurately: the N atoms, as central atoms, contain only one pair of lone electrons, while O/S/Se atoms have two pairs of lone electrons. Since lone pairs occupy more space than bonding pairs, and the repulsion between lone pairs is the strongest (repulsion order: lone pair–lone pair > lone pair–bonding pair > bonding pair–bonding pair), and this enhanced repulsion forces the bonding pairs around O/S/Se atoms to be closer. As a result, the bond angle $C_2–X–C_3$ (X = O/S/Se) is significantly smaller than the bond angle $C_4–N–C_5$ at the N atom position (Fig. 4), similar to how H_2O (104.5°) exhibits a smaller
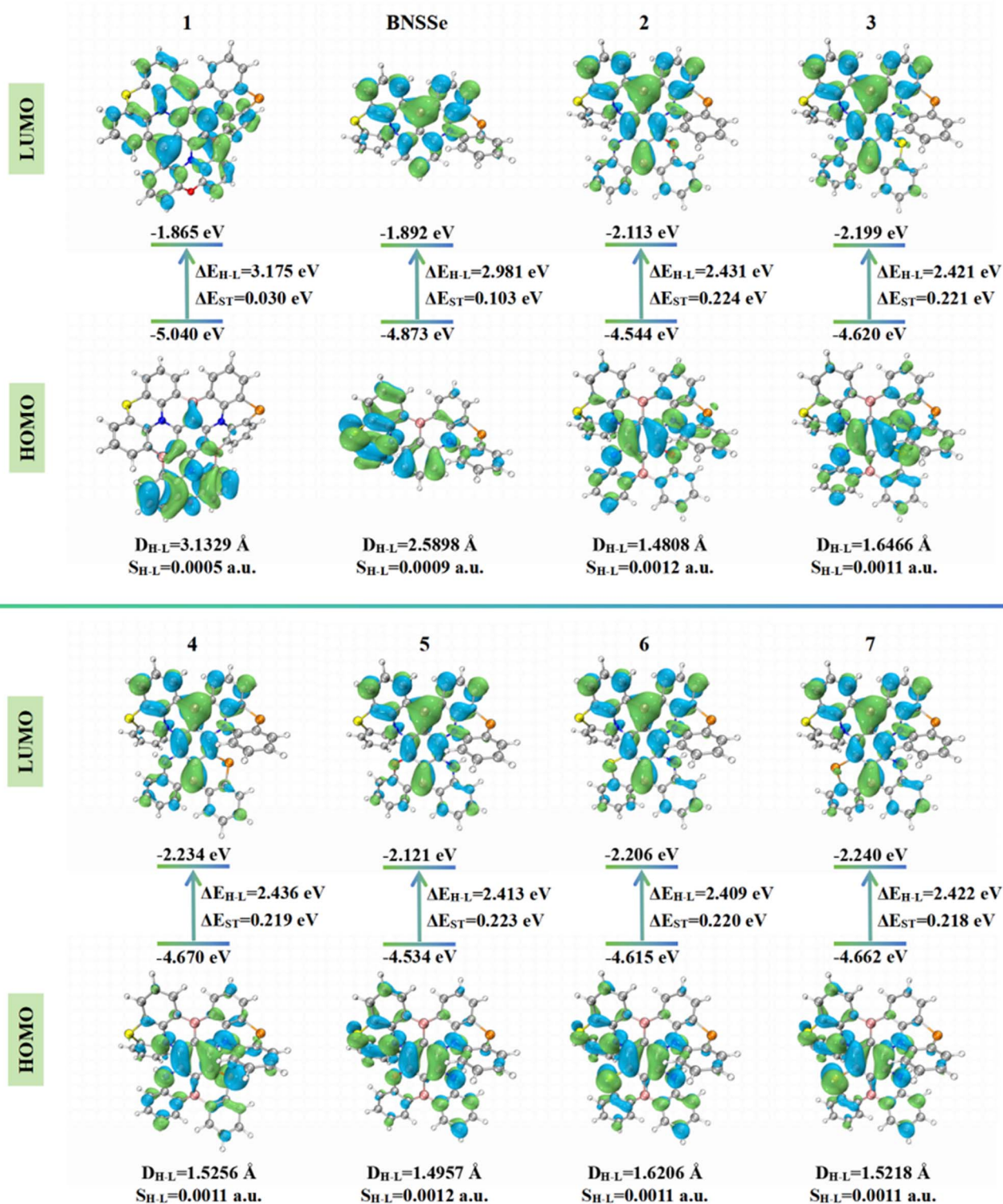
Fig. 3 The energy levels of HOMO and LUMO, ΔE_{H-L}, ΔE_{ST}, and their orbital distributions in the S_1 state of the investigated molecules, as well as the D_{H-L} and S_{H-L} between the HOMO and LUMO in the S_1 state.

bond angle compared to NH_3 (107°). This bond angle compression effect exacerbates the structural distortion of the fragment containing O/S/Se, reducing molecular planarity. Further comparison of two key dihedral angles—the dihedral angle $C_1–C_2–X–C_3$ (θ) on the side with O/S/Se and the dihedral angle $C_1–C_4–N–C_5$ (α) on the side with N—reveals that θ is consistently larger than α. This also confirms that the planarity of the fragment containing O/S/Se is poorer (Fig. S2). Therefore,

the conjugation degree between the six-membered ring containing O/S/Se, adjacent benzene rings, and the central benzene ring is lower than that of the fragment containing N. This hinders the delocalization of the HOMO electron cloud along the axial direction from the O/S/Se-containing fragment to the obliquely upper part, making the HOMO delocalization more inclined to the axial direction from the N-containing fragment to the obliquely upper part. As a result, in molecules **2–4**, the HOMO electron cloud is more distributed on the Se atom of the main skeleton. In contrast, in molecules **5–7**, the HOMO is barely distributed on the Se atom of the main skeleton (Fig. 5). It is generally accepted that the magnitude of SOC is proportional to the fourth power of the nuclear charge number (Z^4).[14] As a fourth-period element, the contribution of Se to the excited-state transition orbitals will greatly affect the SOC and RISC rate of the molecule. We further calculated the percentage contribution of Se to the hole orbital in the S_1 state of molecules **2–7** using Multiwfn.[55] Since molecules **4** and **7** have an additional Se atom introduced into the original main skeleton, the Se atom on the main skeleton is named Se(1), and the additionally introduced Se atom in our design is named Se(2). According to Table 1, the contribution of Se to the hole in molecules **2–4** ranges from 1.289–15.807%, which is significantly higher than the 0.335–12.661% in molecules **5–7**. Therefore, the higher contribution of Se atoms to the excited-

state transition orbitals in molecules **2–4** endows them with a stronger heavy atom effect, indicating that they will have larger SOC constants and faster RISC rates.

3.2 Absorption and emission spectra

Based on the optimized geometric structures of the ground and excited states, we conducted a systematic theoretical calculation study on the electronic transition properties of each molecule. Table 2 details the key parameters of absorption and emission spectra, including wavelength, vertical excitation energy, oscillator strength (f), and transition configuration, which are compared and verified with experimental value. The results show that the emission wavelength of the parent molecule **BNSSe** calculated by the TDDFT/B3LYP-D3(BJ) method is 504 nm, which is highly consistent with the experimental value of 520 nm, verifying the reliability of the calculation method. The lowest absorption and emission transitions of the studied molecules are mainly derived from the HOMO → LUMO electronic transition, which further confirms the effectiveness of our previous strategy for predicting spectral redshift and blue-shift by regulating FMOs.

More importantly, the calculation results clearly reveal the regulation law of molecular structure on emission color: molecule **1** successfully achieves blue emission (469 nm) by introducing the *para*-B–π–N structure, while molecules **2–7**
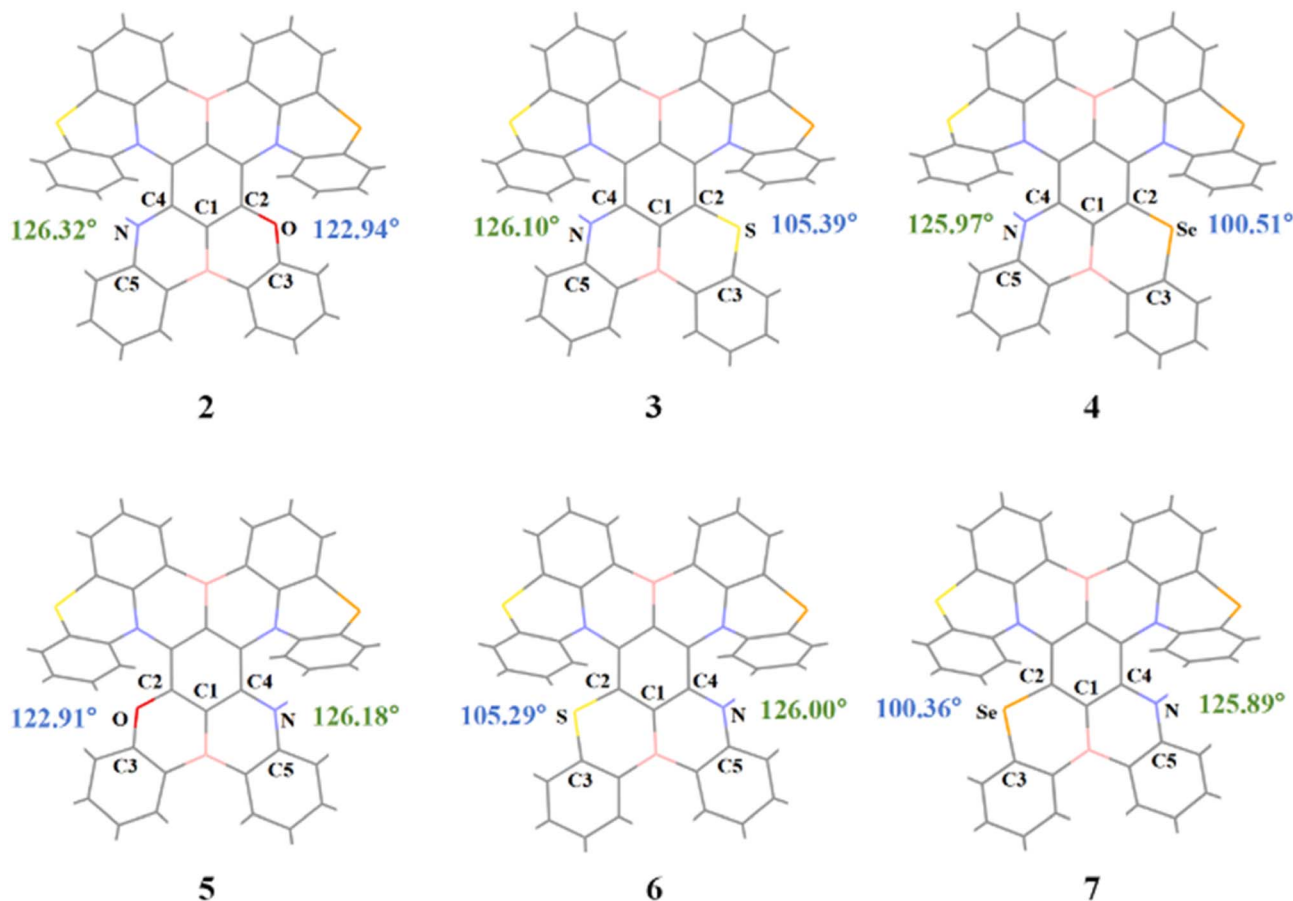

Fig. 4 Geometric structures of the S_1 state and key bond angle C_2–X–C_3 and C_4–N–C_5 parameters of the investigated red emitters.
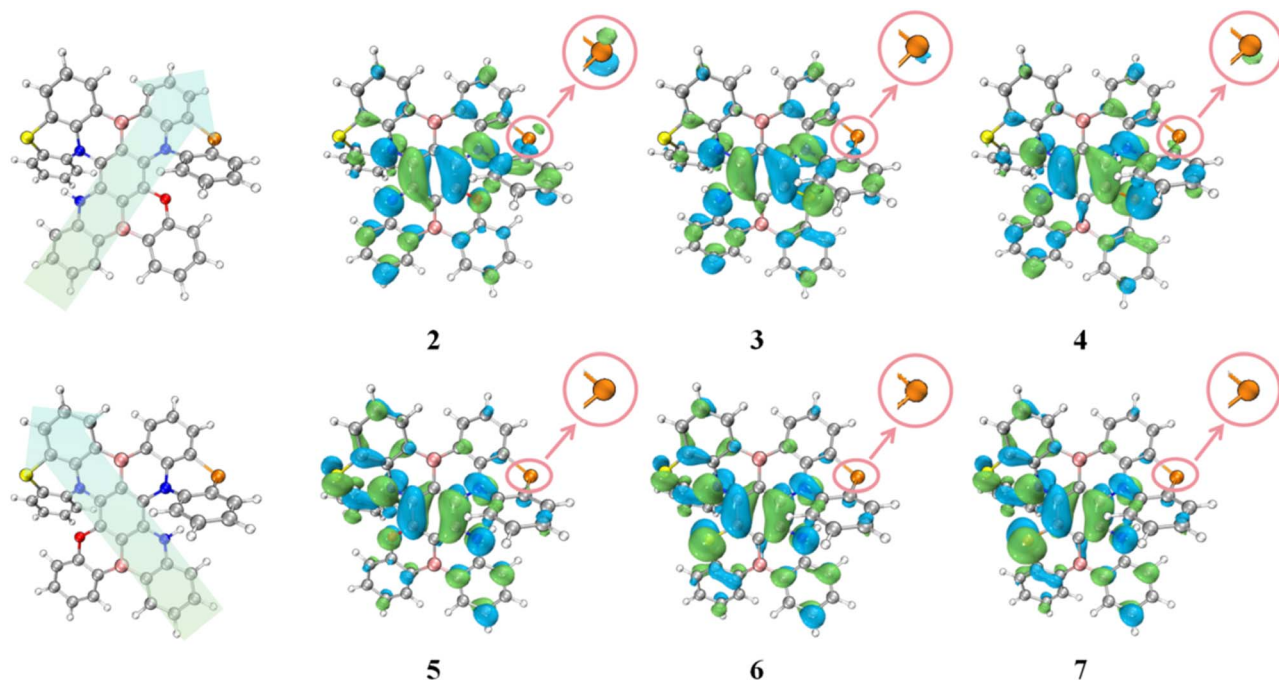
Fig. 5 The axial schematic diagram and actual distribution map of the HOMO electron cloud of the investigated red emitters in the S_1 state; enlarged view: the HOMO distribution of the Se segment in the main framework.

adopt the *para*-B–π–B and N–π–D (donor D = N/O/S/Se) structures, with emission wavelengths redshifted to the range of 627–634 nm, showing pure red fluorescence characteristics (Fig. 6). These results not only verify the prediction of FMO analysis but also confirm the feasibility of designing blue and red MR-TADF materials by precisely regulating molecular structures. Most importantly, the blue emission (469 nm) of molecule **1** and red emission (627–634 nm) of molecules **2–7** designed by us are highly consistent with the blue (467 nm) and red (630 nm) standards defined by BT.2020 announced by the International Telecommunication Union (ITU).[24] This finding provides theoretical guidance for developing high-performance narrowband luminescent materials that meet the standards of the display industry, and also opens up new research ideas for designing high-performance MR-TADF materials with a wide color gamut through precise regulation of electronic structures.

3.3 Excited state radiative and non-radiative transition rates

We know that the luminescence mechanism of TADF materials is very complex, involving radiative and non-radiative transitions of fluorescence and phosphorescence, as well as ISC and RISC processes between S_1 and T_1 states. To achieve high-

performance TADF materials, several key conditions must be met simultaneously: fast fluorescence radiative decay, efficient RISC process, slow phosphorescence radiation, and significantly suppressed non-radiative decay. Based on this understanding, our research is not only committed to regulating the emission color of MR-TADF molecules. More importantly, through quantitative calculation of the mutual conversion rates between various electronic states and their competitive relationships, we systematically optimize these key luminescence processes to achieve higher luminescence efficiency. This research idea of multi-parameter synergistic optimization provides a comprehensive theoretical basis for the development of high-performance TADF materials.

3.3.1 Radiative and non-radiative transitions of $S_1 \rightarrow S_0$. According to Einstein's spontaneous emission equation (formula (1)), the prompt fluorescence radiative transition rate (k_r^S) is related to the vertical excitation energy and f of the $S_1 \rightarrow S_0$ transition process of the studied molecule. The f is proportional to the transition energy ($E_j - E_i$) between the two states and the square of the transition dipole moment ($|\mu|^2$).[56]

$$f_{ij} = \tfrac{2}{3}(E_j - E_i)|\mu_{ij}|^2 \tag{14}$$

The magnitude of the transition dipole moment depends on the overlap integral of the wavefunctions of the S_1 and S_0 states. If the transition mainly corresponds to the electronic excitation from the HOMO to LUMO, it can be approximately equivalent to the spatial overlap degree of the HOMO and LUMO orbitals.[57,58]

$$\mu_{S_1-S_0} = |\langle \psi_{S_1} | \bar{\mu} | \psi_{S_0} \rangle| \approx |\langle L | \bar{\mu} | H \rangle| \propto S_{[H/L]} \tag{15}$$

Table 1 The contribution percentage (%) of Se to the hole orbital in the S_1 state of the investigated red emitters

	2	3	4	5	6	7
Se(1)	2.198	1.289	1.389	0.402	0.335	0.333
Se(2)	—	—	14.418	—	—	12.328
Se(sum)	2.198	1.289	15.807	0.402	0.335	12.661

Table 2 Data on the absorption and fluorescence transition processes of the investigated molecules, along with the corresponding experimental value

	Electronic transition	Vertical excitation energy (eV)	λ (nm)	f	Configuration	
Absorption						
1	$S_0 \rightarrow S_1$	2.787	445	0.0477	HOMO $\rightarrow$ LUMO	71%
					HOMO-1 $\rightarrow$ LUMO+1	17%
					HOMO $\rightarrow$ LUMO+1	4%
					HOMO-2 $\rightarrow$ LUMO+1	3%
BNSSe	$S_0 \rightarrow S_1$	2.799	443	0.2145	HOMO $\rightarrow$ LUMO	98%
2	$S_0 \rightarrow S_1$	2.212	561	0.1590	HOMO $\rightarrow$ LUMO	99%
3	$S_0 \rightarrow S_1$	2.191	566	0.1466	HOMO $\rightarrow$ LUMO	99%
4	$S_0 \rightarrow S_1$	2.194	565	0.1430	HOMO $\rightarrow$ LUMO	99%
5	$S_0 \rightarrow S_1$	2.200	564	0.1571	HOMO $\rightarrow$ LUMO	99%
6	$S_0 \rightarrow S_1$	2.183	568	0.1444	HOMO $\rightarrow$ LUMO	99%
7	$S_0 \rightarrow S_1$	2.188	567	0.1412	HOMO $\rightarrow$ LUMO	99%
Fluorescence						
1	$S_1 \rightarrow S_0$	2.646	469	0.0716	HOMO $\rightarrow$ LUMO	82%
					HOMO $\rightarrow$ LUMO+1	7%
					HOMO-1 $\rightarrow$ LUMO+1	5%
BNSSe	$S_1 \rightarrow S_0$	2.459	504/520[a]	0.1567	HOMO $\rightarrow$ LUMO	99%
2	$S_1 \rightarrow S_0$	1.976	627	0.1263	HOMO $\rightarrow$ LUMO	99%
3	$S_1 \rightarrow S_0$	1.965	631	0.1195	HOMO $\rightarrow$ LUMO	99%
4	$S_1 \rightarrow S_0$	1.977	627	0.1209	HOMO $\rightarrow$ LUMO	99%
5	$S_1 \rightarrow S_0$	1.962	632	0.1264	HOMO $\rightarrow$ LUMO	99%
6	$S_1 \rightarrow S_0$	1.954	634	0.1194	HOMO $\rightarrow$ LUMO	99%
7	$S_1 \rightarrow S_0$	1.964	631	0.1201	HOMO $\rightarrow$ LUMO	99%

[a] Experimental value from ref. 18.

where ψ_{S_0/S_1} denotes the electronic wave functions of the S_0/S_1 state and $S_{[H/L]}$ denotes the spatial overlap between the HOMO and LUMO wave functions.

To design blue emission MR-TADF molecules with fast RISC rates and thereby suppress the efficiency roll-off of blue emission devices, molecule **1** achieves π-extension by introducing a rigid B/N-fused ring structure, forming hybrid SRCT/LRCT characteristics. Its CT character is significantly enhanced compared to the parent molecule **BNSSe** (which exhibits SRCT characteristics). This design strategy reduces the overlap degree between the HOMO and LUMO of molecule **1** (molecule **1**: 0.0005 a.u.; **BNSSe**: 0.0009 a.u.), leading to a remarkable decrease in its ΔE_{ST} (molecule **1**: 0.030 eV; **BNSSe**: 0.103 eV), which is conducive to improving the RISC rate. However, the reduced HOMO–LUMO overlap inevitably results in decreases in the transition dipole moment and oscillator strength (Table S2), ultimately leading to a lower prompt fluorescence radiative transition rate of blue emission molecule **1** compared to **BNSSe** (Table 3). On the other hand, by introducing the *para*-B–π–N structure, molecule **1** successfully achieves blue emission, with a vertical excitation energy (2.885 eV) significantly higher than that of the green emission molecule **BNSSe** (2.710 eV). This ensures that its k_r^S remains on the same order of magnitude as
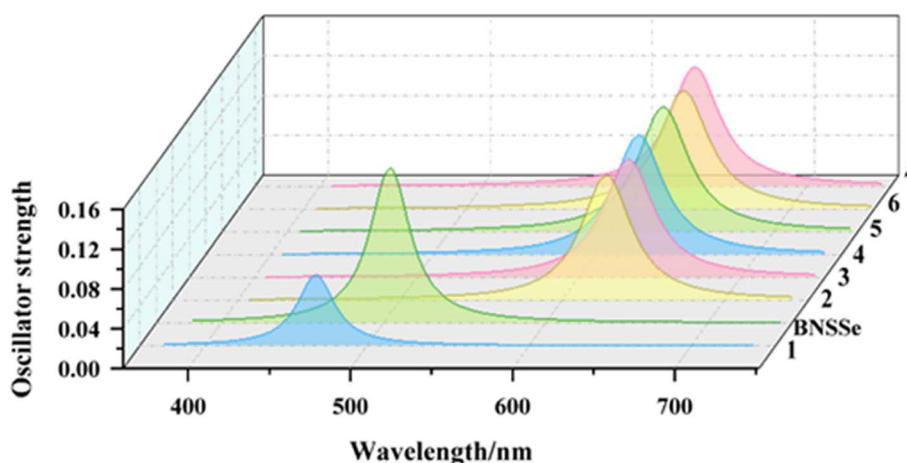

Fig. 6 Emission spectra of the investigated molecules.

Table 3 Photophysical properties characterizing $S_1 \rightarrow S_0$ emission: vertical excitation energy, oscillator strength (f), k_r^S, and lifetimes (τ)

	Vertical excitation energy/eV	f	k_r^S/s^{-1}	$\tau/\mu s$
1	2.885	0.0716	2.58×10^7	0.039
BNSSe	2.710	0.1567	4.99×10^7	0.020
2	2.121	0.1263	2.46×10^7	0.041
3	2.114	0.1195	2.32×10^7	0.043
4	2.126	0.1209	2.37×10^7	0.042
5	2.112	0.1264	2.44×10^7	0.041
6	2.105	0.1194	2.29×10^7	0.044
7	2.116	0.1201	2.33×10^7	0.043

BNSSe (molecule **1**: 2.58×10^7 s^{-1}; **BNSSe**: 4.99×10^7 s^{-1}), indicating favorable fluorescence performance.

In addition, to achieve the design goal of pure red emission MR-TADF molecules, we successfully tuned the emission spectrum to around 630 nm by introducing *para*-B–π–B and N–π–D (donor D = N/O/S/Se) structures into the main skeleton of the parent molecule **BNSSe**. However, the significant red-shift of the emission spectrum inevitably leads to a substantial reduction in the vertical excitation energy of molecules **2**–**7** compared to **BNSSe**, ultimately resulting in a decrease in their k_r^S. Notably, despite the lower k_r^S relative to **BNSSe**, it still maintains the order of magnitude of 10^7 s^{-1}, which is comparable to representative high-efficiency red emission materials reported in the literature (Table S3). This fast fluorescence radiative characteristic makes it promising to break through the limitations of the traditional energy gap law.

According to the energy gap law, the non-radiative transition rate of $S_1 \rightarrow S_0$ (k_{nr}^S) depends exponentially on the energy gap between the S_0 and S_1 states. A large energy gap between S_0/S_1 states and a small electron-vibration coupling parameter can both suppress k_{nr}^S. Here, we express this using a simple approximate relationship.[21,59,60]

$$k_{nr}^S \sim \exp(-\beta \Delta E) \tag{16}$$

where ΔE represents the energy gap between the S_0 and S_1 states, and β is the electron-vibration coupling parameter

between S_0 and S_1 states. The electron-vibration coupling parameter is considered herein through the reorganization energy (λ) between the ground and excited states. λ is a core parameter describing electron transfer processes in Marcus theory, which quantitatively characterizes the energy change of the system caused by molecular geometric relaxation after electronic state transition. In the above formula, the smaller the λ, the smaller the k_{nr}^S.

In the development of OLED materials, the energy gap law has long been a key bottleneck restricting the performance improvement of red emitters. This forces material designers to make trade-offs between luminous efficiency and red emission characteristics. To break this limitation, this study successfully achieved effective suppression of non-radiative transition processes through an innovative molecular design strategy. The results show that compared with the parent molecule **BNSSe** (the reorganization energies of the S_1 and S_0 potential energy surfaces are defined as λ_1 and λ_2, respectively, with $\lambda_1 = 1632$ cm^{-1} and $\lambda_2 = 1303$ cm^{-1}), in the designed red emitters **2**–**7**, although the ΔE values are smaller, the λ values between S_1 and S_0 states (Fig. 7 and Table 4, with $\lambda_1 = 939$–1022 cm^{-1} and $\lambda_2 = 858$–922 cm^{-1}) are significantly reduced through careful regulation of molecular structure. To our surprise, despite the significant decrease in ΔE (approximately 0.653 eV/5267–0.674 eV/5436 cm^{-1}), which should have led to an exponential increase in k_{nr}^S according to the energy gap law, the actually measured k_{nr}^S did not increase but instead decreased. This phenomenon indicates that although the reduction in λ is limited (for example, λ_1 and λ_2 of molecule **2** decreased by 612 cm^{-1} and 397 cm^{-1}, respectively), its inhibitory effect on k_{nr}^S almost completely offsets the promoting effect caused by the decrease in ΔE. This striking contrast demonstrates that within this energy level range, k_{nr}^S is extremely sensitive to changes in λ, and λ becomes the key factor dominating the non-radiative transition process. This breakthrough improvement stems from the unique molecular structure design: fusing another MR molecular skeleton (DOBNA derivative) with the central benzene ring in the **BNSSe** main skeleton, forming a hybrid π-bonding/non-bonding molecular orbital co-constructed by the central benzene ring and B, N, and X (X = O/S/Se) units. This
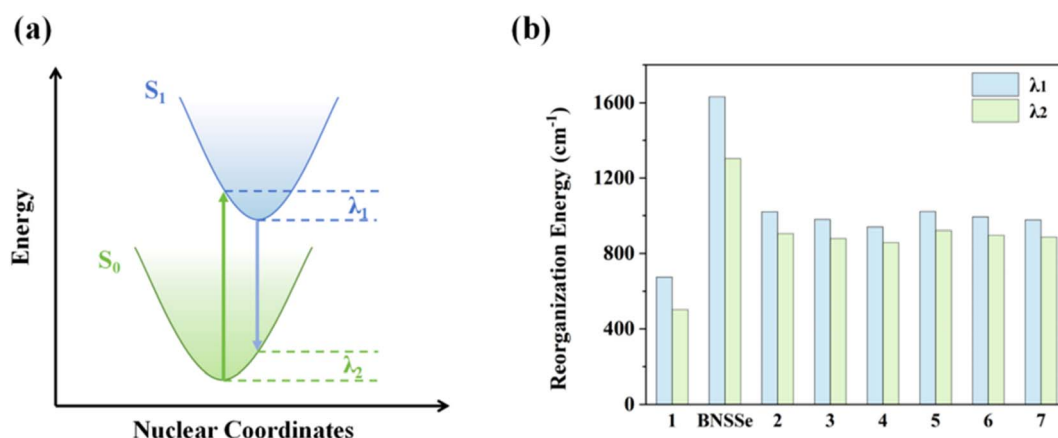

Fig. 7 (a) Schematic diagram of the reorganization energy between the S_1 and S_0 states. (b) Bar charts of λ_1 and λ_2 for the investigated molecules.

Table 4 Key photophysical parameters (ΔE, λ, k_{nr}^S) for the $S_1 \rightarrow S_0$ transition

	ΔE/eV	λ_1/cm^{-1}	λ_2/cm^{-1}	k_{nr}^S/s^{-1}
1	3.037	675	503	1.06×10^3
BNSSe	2.974	1632	1303	8.65×10^6
2	2.321	1020	906	3.50×10^6
3	2.310	979	879	4.87×10^6
4	2.303	939	858	6.40×10^6
5	2.317	1022	922	2.68×10^6
6	2.305	993	897	6.42×10^6
7	2.300	977	888	1.15×10^7

effectively suppresses structural relaxation between S_1 and S_0 states. A significant effect of this structural regulation is reflected in the remarkable reduction of k_{nr}^S. Calculation data show that although the ΔE values of red emitters **2–7** are relatively small, their k_{nr}^S values are much smaller than the corresponding k_r^S (Tables 3 and 4). This means these materials are expected to achieve high luminous efficiency and break through the limitations of the energy gap law.

It is worth noting that a similar molecular design strategy also has significant effects in blue-emitting materials. Molecule **1** reduces λ_1 and λ_2 to 675 cm^{-1} and 503 cm^{-1}, respectively, through the extended B/N fused-ring structure. Combined with its large ΔE, the k_{nr}^S of $S_1 \rightarrow S_0$ is as low as 1.06×10^3 s^{-1}, which will greatly improve its luminous efficiency and provide a new design idea for developing high-efficiency blue-emitting materials. These findings not only provide new insights into understanding the relationship between molecular structure and luminous performance but also offer new perspectives for developing high-performance OLED luminescent materials.

Studies have shown that in addition to the non-radiative transition rate, the FWHM of the emission spectrum is also affected by the reorganization energy of the S_0 state potential energy surface (λ_2).[61] To further investigate the k_{nr}^S of the studied molecules and determine whether the molecules designed herein possess narrowband emission characteristics, we decomposed λ_2 into contributions from each normal mode. The displacement vectors corresponding to the normal modes with the largest contributions in the low-frequency and high-frequency regions are also marked in Fig. S3 and S4. It can be seen that the reorganization energies in both the low-frequency and high-frequency regions of the parent molecule **BNSSe** mainly originate from the bending vibrations of the entire molecular skeleton. Compared with **BNSSe**, the reorganization energy vibration modes of molecules **1–7** are significantly reduced, indicating that their geometric structural relaxation is well suppressed, suggesting that all designed molecules can maintain good narrowband emission characteristics. The reorganization energies in the low-frequency and high-frequency regions of molecule **1** mainly come from the stretching vibrations of the molecular skeleton and the bending vibrations of C–H bonds. For molecules **2–7**, the low-frequency reorganization energy arises from the bending vibrations of C–H bonds in the peripheral benzene rings, while the high-frequency reorganization energy mainly comes from the bending vibrations of

C–H bonds in the peripheral benzene rings and the stretching vibrations of the central benzene ring and surrounding six-membered rings.

In addition, the sources of reorganization energy λ_2 were decomposed into contributions from bond lengths, bond angles, and dihedral angles. The reorganization energy of **BNSSe** mainly comes from dihedral angles, while that of molecules **1–6** is mainly from bond lengths, with their k_{nr}^S significantly lower than that of the parent molecule. Notably, when observing the two groups of molecules **2–4** and **5–7**, as the atomic radii of O, S, and Se increase, the contribution of bond lengths to reorganization energy gradually decreases, while that of dihedral angles gradually increases. Correspondingly, their k_{nr}^S also increases. Therefore, we speculate that in the total reorganization energy, contributions from dihedral angles can more significantly enhance electron-vibration coupling and structural relaxation. In particular, consistent with **BNSSe**, the reorganization energy of molecule **7** also mainly comes from dihedral angles, and its k_{nr}^S is even larger than that of the parent molecule. On the one hand, this is because molecule **7** has the smallest ΔE, which significantly increases k_{nr}^S. On the other hand, it may be due to the vibrations from dihedral angles that enhance structural relaxation. Thus, for this system, reducing the reorganization energy contributed by dihedral angles may be an effective method to suppress structural relaxation and non-radiative decay.

3.3.2 RISC between T_1 and S_1 states. RISC is the rate-determining step in the luminescence process of TADF molecules, and the key to developing high-performance TADF materials lies in achieving a fast RISC rate. In this study, the theoretical formulae proposed by Katsuyuki Shizu and Hironori Kaji[48] (formulae (2)–(4)) were adopted to calculate the k_{ISC} and k_{RISC} of the molecules. Relevant ΔE_{ST} and SOC data are summarized in Table 5. According to the formulae, either reducing ΔE_{ST} or increasing SOC can effectively enhance k_{RISC}, which are the core approaches to optimizing RISC dynamics. Combined with the aforementioned frontier molecular orbital analysis, compared with the parent molecule **BNSSe** with SRCT characteristics ($D_{H-L} = 2.5898$ Å, $S_{H-L} = 0.0009$ a.u.), molecule **1** achieves a D_{H-L} increased to 3.1329 Å and an S_{H-L} reduced to 0.0005 a.u. via the introduction of SRCT/LRCT hybrid characteristics, ultimately leading to a significant decrease in ΔE_{ST} (from 0.103 eV to 0.030 eV). In addition, compared with **BNSSe**, molecule **1** exhibits a remarkable enhancement in SOC, providing additional support for the increase in k_{RISC}. Under the synergistic effect of reduced ΔE_{ST} and enhanced SOC, the k_{RISC} of molecule **1** is more than 1000 times higher than that of the parent molecule **BNSSe**, reaching an excellent level of the order of 10^8 s^{-1}. This value not only significantly surpasses those of traditional MR-TADF molecules (generally <10^5 s^{-1}) but is also comparable to those of high-performance metal complexes.[9,14,62–65] Such outstanding RISC characteristics can promote a faster TADF rate, allow more short-lived excited states to actively participate in the luminescence process, and help reduce material degradation caused by triplet exciton accumulation. In addition, we also accurately evaluated the

Table 5 Values of ΔE_{ST}, SOC and k_{ISC} and k_{RISC} calculated at room temperature for the investigated molecules

	$\Delta E_{ST}/eV$	$SOC(S_1–T_1)/cm^{-1}$	k_{ISC}/s^{-1}	k_{RISC}/s^{-1}
1	0.030	1.69	1.74×10^9	1.80×10^8
BNSSe	$0.103/0.120^a$	0.38	$2.85 \times 10^7/2.90 \times 10^{8a}$	$1.77 \times 10^5/6.00 \times 10^{5a}$
2	0.224	0.67	2.39×10^7	1.39×10^3
3	0.221	0.64	2.23×10^7	1.45×10^3
4	0.219	3.17	5.62×10^8	3.92×10^4
5	0.223	0.25	3.37×10^6	2.00×10^2
6	0.220	0.22	2.74×10^6	1.84×10^2
7	0.218	2.68	4.05×10^8	2.93×10^4

^{a} Experimental values from ref. 18.

degree of suppressed efficiency roll-off by means of the figure of merit (FOM) proposed by S. Diesing *et al.*[66]

$$FOM = k_r^S K_{eq} = \frac{4k_r^S k_{RISC}}{3k_r^S + 4k_{ISC}} \tag{17}$$

According to the data in Table S4, the figure of merit (FOM) of molecule **1** is significantly enhanced compared to that of **BNSSe**. This demonstrates that the efficiency roll-off of the designed blue emission MR-TADF molecule is remarkably suppressed, providing an effective strategy for addressing the efficiency roll-off issue of such materials. These results confirm that introducing SRCT/LRCT hybrid characteristics *via* the rigid B/N-fused ring structure can effectively reduce the molecular ΔE_{ST} and enhance k_{RISC}, providing an important design strategy for the development of high-efficiency MR-TADF materials.

For the designed red emitters **2–7**, enhanced SRCT characteristics lead to decreased $D_{H–L}$ and increased $S_{H–L}$, resulting in the ΔE_{ST} increasing to approximately 0.2 eV and the k_{RISC} being lower than that of **BNSSe**. Fortunately, molecules **4** and **7** exhibit significantly enhanced SOC through the heavy-atom effect of dual Se incorporation, achieving k_{RISC} on the order of 10^4 s^{-1} and establishing them as high-performance red-emitting MR-TADF materials (Table S3). Further comparison of the structure–performance relationships between molecules **2/5**, **3/6**, and **4/7** reveals that differences in the spatial positions of O/S/Se heteroatoms cause significant changes in SOC, thereby affecting the magnitude of k_{RISC}. This calculation result confirms the previous theoretical prediction: changing only the spatial positions of heteroatoms (O/S/Se) causes changes in molecular geometric structure, which drives the axial distribution rearrangement of frontier molecular orbitals, thereby directionally altering the contribution of main skeleton Se atoms to excited-state transition orbitals, ultimately leading to obvious differences in SOC and RISC rates.

Notably, for molecules containing only one Se atom (**2/5**, **3/6**), changing the spatial position of the heteroatom can increase k_{RISC} by an order of magnitude. For molecules **4** and **7** with two Se atoms, however, the increase in k_{RISC} is relatively limited. This indicates that the strategy of enhancing k_{RISC} by regulating heteroatom spatial positions is more effective for molecules with a single Se atom introduced. Although bis-Se molecules (**4/**

7) exhibit better k_{RISC} (10^4 s^{-1}), considering that Se-containing reagents generally have high toxicity and poor stability, the synthesis of organic Se compounds often faces great challenges.[67] In practical applications, a balance must be struck between the number of Se atoms and performance gains. In recent years, researchers have developed various new selenium reagents with better stability, low toxicity, and easy availability, making the synthesis of various organic Se compounds more feasible. However, in the development of MR-TADF materials, it remains important to maximize the heavy atom effect while minimizing Se atom usage. The heteroatom site regulation strategy proposed in this study provides an effective solution to this key issue.

3.3.3 Radiative and non-radiative transitions of $T_1 \rightarrow S_0$. There are three decay pathways for T_1 state excitons: phosphorescent radiative transition from $T_1 \rightarrow S_0$, non-radiative transition from $T_1 \rightarrow S_0$, and RISC process from $T_1 \rightarrow S_1$. To ensure that T_1 state excitons can smoothly upconvert to the S_1 state for TADF emission, $k_{RISC} \gg (k_rT + k_{nr}^T)$ is required. We calculated the phosphorescence rate (k_r^T) using the Einstein spontaneous emission equation, with relevant data summarized in Table S5. Since phosphorescence involves radiative transitions between electronic states of different multiplicities, we used the ORCA 5.0 program to obtain the corresponding transition oscillator strengths of $T_1 \rightarrow S_0$ after considering SOC perturbation. Due to the weak f values, the k_r^T values of all studied molecules are very low. The k_r^T values of **BNSSe** and designed molecules **1–7** are 1.47×10^2 s^{-1}, 1.65×10^3 s^{-1}, 1.63×10^1 s^{-1}, 1.41×10^1 s^{-1}, 2.44×10^3 s^{-1}, 2.00×10^1 s^{-1}, 1.80×10^1 s^{-1} and 2.48×10^2 s^{-1}, respectively.

The non-radiative transition rate of $T_1 \rightarrow S_0$ was calculated using formula (5). The k_{nr}^T values of **BNSSe** and designed molecules **1–7** are 2.64×10^1 s^{-1}, 3.96×10^2 s^{-1}, 1.89 s^{-1}, 7.27×10^{-1} s^{-1}, 1.43×10^2 s^{-1}, 1.12 s^{-1}, 2.47 s^{-1} and 2.01×10^2 s^{-1}, respectively. Data in Table S6 show that molecules **1**, **4**, and **7** exhibit a significant SOC enhancement effect between T_1 and S_0 states, with coupling constants of 28.74 cm^{-1}, 12.17 cm^{-1}, and 14.41 cm^{-1}, respectively. These are significantly higher than that of the parent molecule **BNSSe** (7.04 cm^{-1}), a characteristic that leads to a corresponding increase in their non-radiative transition rates. In addition, the large structural distortion between the T_1 and S_0 states of molecules **4** and **7** also indicates

that they will dissipate part of the energy (Fig. 2). Fortunately, excited-state dynamics analysis reveals that the k_{RISC} of these molecules is significantly higher than the corresponding k_{nr}^T (Tables 5 and S6). This rate advantage ensures that T_1 state excitons can effectively upconvert to the S_1 state, thereby maintaining an efficient TADF process.

3.3.4 TADF quantum efficiency. Based on the above systematic analysis, we summarized the TADF luminescence mechanism of the studied molecules and calculated the corresponding TADF quantum efficiency (ϕ_{TADF}) (Fig. 8 and S5). The ϕ_{TADF} values of the parent molecule **BNSSe** and designed molecules **1–7** are 27.85%, 76.47%, 39.26%, 35.95%, 32.28%, 8.91%, 5.94%, and 50.67%, respectively. Among them, the blue emitter **1** exhibits the optimal combination of photophysical properties: it has the lowest k_{nr}^S (1.06×10^3 s^{-1}) and the highest k_{RISC} (1.80×10^8 s^{-1}), while maintaining a high k_r^S (2.58×10^7 s^{-1}). This ideal rate balance significantly enhances its ϕ_{TADF}. For red emitters, relying on the heteroatom site regulation strategy, the larger k_{ISC} and k_{RISC} of molecules **2–4** increase ϕ_{TADF} to approximately 30%. In contrast, the smaller k_{ISC} and k_{RISC} of molecules **5** and **6** hinder the efficient return of triplet excitons to the singlet state for delayed fluorescence emission, ultimately leading to a decrease in ϕ_{TADF}. However, it is worth noting that the ϕ_{TADF} of molecule **7** is higher than that of the corresponding molecule **4**. On the one hand, this is because the heteroatom site regulation strategy has a limited effect on molecules with double Se atoms introduced. On the other hand, the phosphorescence rate of molecule **4** is an order of magnitude higher than that of molecule **7**; the competition from the phosphorescence process reduces its TADF contribution. Therefore, in the design of Se-containing MR-TADF materials, it is necessary

to not only consider the SOC enhancement effect but also balance the competition between different radiative and non-radiative channels to achieve optimal luminescence performance.

3.4 Theoretical prediction of the emission spectrum FWHM

In terms of theoretical prediction of the spectral FWHM, this study adopted a dual verification strategy combining theoretical calculations and deep learning for systematic evaluation. First, vibrationally resolved emission spectra of each molecule were calculated using MOMAP software, and FWHM values were extracted from them (Fig. S6 and S7). The calculated FWHM for the parent molecule **BNSSe** is 59 nm, closely matching the experimental value of 50 nm. Notably, the designed molecules **1–7** also exhibit narrowband emission, with calculated FWHM values of 32, 57, 60, 62, 59, 65 and 65 nm, all falling within the narrowband regime below 70 nm. This demonstrates successful modulation of emission color and decay rates without compromising the narrowband linewidth.

To further verify this result, we also used the SOGCN model based on a graph convolutional neural network independently developed by our research group to predict the FWHM of these molecules (Table S7).[20] The model predicts the FWHM of **BNSSe** to be 56 nm, which is highly consistent with the experimental value, fully verifying the reliability of the model. Strikingly, the SOGCN model predicts that the FWHM values of molecules **1–7** are stable around 40 nm, showing a systematic difference from the MOMAP calculation results but with a consistent trend. This difference may stem from the different handling of molecular vibration modes by the two methods: MOMAP is based on
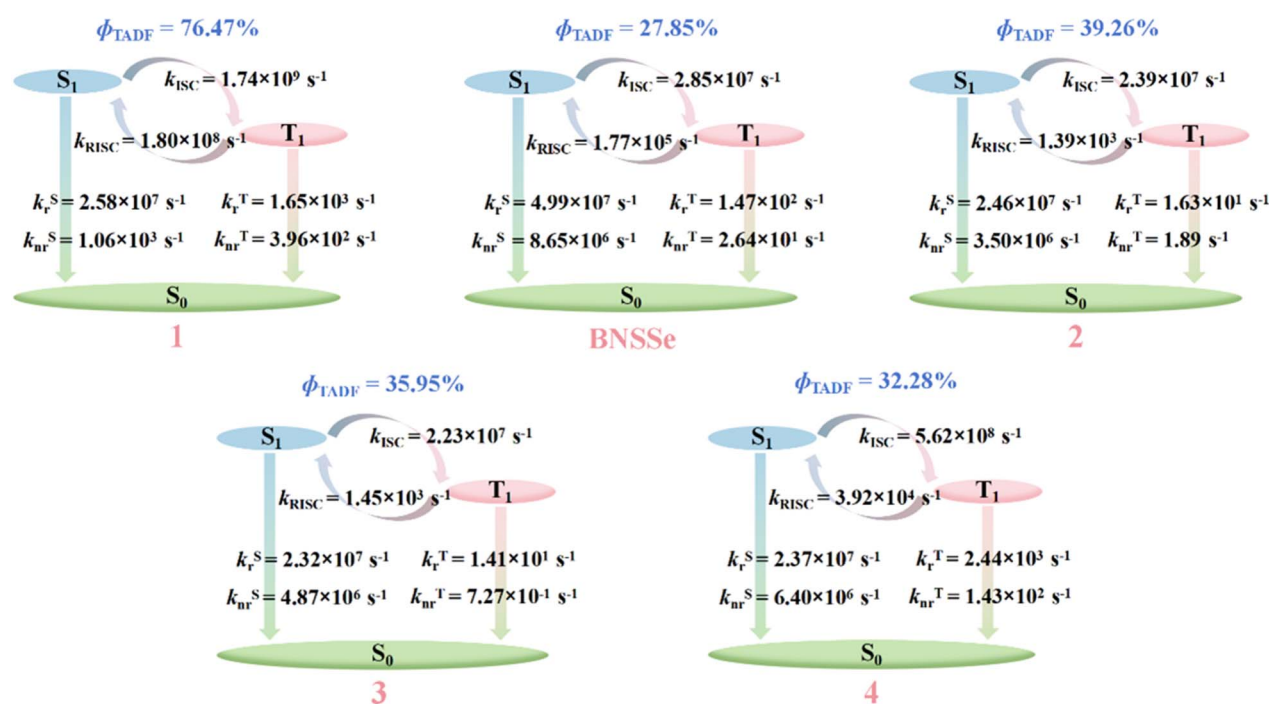

Fig. 8 Relevant transition rates and ϕ_{TADF} at room temperature for the investigated molecules **BNSSe** and **1–4**.

precise vibrationally resolved calculations, while SOGCN captures the correlation between the molecular structure and spectrum through a data-driven approach.

The conclusions drawn by the two methods mutually confirm each other, jointly revealing the success of the molecular design: by introducing rigid fused-ring structures and enhancing SRCT characteristics, excited-state structural relaxation is effectively suppressed, leading to reduced reorganization energy. This dual-track verification mode of "computational simulation + AI prediction" confirms the excellent performance of the designed molecules in maintaining narrowband emission from different perspectives.

3.5 Red emitter design strategy

Based on the structure of the parent molecule **BNSSe**, the blue emitter **1** synergistically weakens the electron-withdrawing/donating abilities of B/N atoms through a modification strategy involving three sets of *para*-B–π–N. This causes the LUMO energy level to rise and the HOMO energy level to drop, significantly widening ΔE_{H-L}, with the emission wavelength blue-shifted to 469 nm. To prepare pure red emitters meeting the BT.2020 standard, it is necessary to synergistically enhance the electron-withdrawing/donating abilities of B/N atoms to reduce ΔE_{H-L}. Therefore, we attempted to replace the lower N and B atoms with each other based on the structure of molecule **1**, designing molecule **1-a** (Fig. S8). Molecule **1-a** exhibits SRCT characteristics, which are beneficial for suppressing electron-vibration coupling and structural relaxation. Thus, the reorganization energy between the S_0 and S_1 states is slightly lower than that of the molecule **BNSSe** (Fig. S9 and Table S8). However, due to the structural arrangement of two sets of N–π–N and one set of B–π–B significantly enhancing the electron-withdrawing/donating abilities of B/N atoms, and the π-expanded structure of rigid fused rings increasing conjugation, the emission spectrum of molecule **1-a** is redshifted to 703 nm. The extremely small emission energy gap leads to a significant increase in the non-radiative transition rate, exceeding the fluorescence radiative rate and causing severe luminescence quenching (Fig. S10).

Based on the above results, we adjusted the design strategy. Studies have shown that in traditional polycyclic aromatic hydrocarbons without B/N heteroatoms, the HOMO and LUMO are mainly concentrated in the π-bond regions formed between atoms. In this case, the bonding/antibonding characteristics enhance electron-vibration coupling between S_0 and S_1 states, making excited states prone to deactivation through non-radiative pathways. In MR-TADF materials containing B/N heteroatoms, the HOMO and LUMO are localized on different atoms, minimizing their bonding/antibonding characteristics. The resulting non-bonding molecular orbitals reduce electron-vibration coupling and structural relaxation in the materials. Therefore, we attempted to fuse another MR-TADF molecule (DOBNA) onto the **BNSSe** main skeleton, designing molecule **2-a** (Fig. S8). The D_{H-L} of molecule **2-a** decreases to 0.7941 Å, and S_{H-L} increases to 0.0012 a.u., indicating enhanced SRCT characteristics. Moreover, it forms unique hybrid π-bonding/non-

bonding molecular orbitals using the central benzene ring and B, N, and O units, effectively reducing the reorganization energy between S_0 and S_1 states. This significantly lowers the non-radiative transition rate to 2.48×10^5 s^{-1} (Fig. S9 and Table S8), showing potential to break through the limitations of the energy gap law. However, due to the weak electron-donating ability of O atoms, the introduction of a *para*-N–π–O structural distribution results in a limited redshift of the emission wavelength of molecule **2-a**, reaching only 595 nm, which is far from the 630 nm specified in the BT.2020 standard. To address this, we further attempted to replace the O atom on one side with an N atom with a stronger electron-donating ability, designing molecules **2** and **5**, whose emission wavelengths are successfully regulated to around 630 nm. Additionally, based on molecules **2** and **5**, we replaced the O atom with S and Se atoms (which exhibit heavy atom effects) to design molecules **3** and **6**, and **4** and **7**, all with emission wavelengths of around 630 nm.

Although the designed molecules **1-a** and **2-a** did not meet the expected goals, they provided valuable insights for research on preparing pure red emitters meeting the BT.2020 standard. Furthermore, due to enhanced SRCT characteristics and hybrid π-bonding/non-bonding molecular orbitals, electron-vibration coupling and structural relaxation during the transition process of molecule **2-a** are well suppressed. This is reflected not only in the significant decrease in its non-radiative transition rate but also in the narrowing of the FWHM of its emission spectrum to 48 nm (Fig. S11), providing theoretical guidance for the preparation of high-performance narrowband orange-red-emitting MR-TADF materials.

4 Conclusions

In this study, we conducted an in-depth investigation into the luminescence mechanism of **BNSSe** by employing DFT, TD-DFT, and SCS-CC2 methods. Based on the structure characteristics of **BNSSe**, we successfully designed high-performance blue-emitting and red-emitting MR-TADF materials through precise regulation of molecular structures, and revealed the regulatory mechanism of heteroatom spatial site specificity on excited-state dynamics. The primary conclusions are outlined as follows:

(1) By incorporating a rigid B/N fused-ring structure into the **BNSSe** molecular framework and leveraging hybrid SRCT/LRCT characteristics, molecule **1** was designed to exhibit accelerated RISC. Compared with **BNSSe**, molecule **1** features a smaller ΔE_{ST}, enhanced SOC, and suppressed structural relaxation, collectively contributing to a remarkable increase in k_{RISC} to 10^8 s^{-1} (3 orders of magnitude higher than that of the **BNSSe**). The introduction of three *para*-configured B–π–N units effectively moderates the electron-withdrawing/donating strengths of the B/N atoms, enlarges the ΔE_{H-L}, and regulates spectral blue-shift. This molecular design offers a new strategy for developing efficient and stable blue-emitting MR-TADF materials.

(2) A series of red emitters **2–7** were designed by incorporating *para*-B–π–B and N–π–D (donor D = N/O/S/Se) to synergistically enhance the electron-withdrawing/donating abilities of B/N atoms. Their emission wavelengths are concentrated

around 630 nm, basically meeting the red standard defined by BT.2020. Theoretical calculations confirm that fusing another MR molecular skeleton (DOBNA derivative) with the central benzene ring in the **BNSSe** main skeleton, and forming hybrid π-bonding/non-bonding molecular orbitals using the central benzene ring and B, N, and X (X = O/S/Se) units, can effectively reduce the λ between the S_1 and S_0 states, thereby suppressing structural relaxation. Although the ΔE of red emitters decreases significantly, the inhibitory effect of λ on k_{nr}^S almost completely offsets the promoting effect induced by the decrease in ΔE. Benefiting from this molecular design, their k_{nr}^S is much smaller than k_r^S, creating favorable conditions for breaking through the limitations of the energy gap law. This provides key insights for the precise design of high-performance MR-TADF materials: while regulating the energy gap, efforts should be made to pursue molecular rigidification to minimize λ, thereby synergistically achieving efficient suppression of non-radiative transition channels.

(3) The directional regulation mechanism of heteroatom spatial sites on SOC was revealed: without increasing the number of Se atoms, the axial distribution rearrangement of frontier molecular orbitals is driven by the differences in O/S/Se sites, optimizing the contribution of Se atoms to excited-state transitions, thereby significantly increasing SOC and improving the k_{RISC} of single-Se molecules by an order of magnitude. This finding goes beyond the cognitive framework of traditional heavy atom effects, providing important theoretical guidance for in-depth understanding of the intrinsic mechanism between SOC enhancement and RISC rate improvement.

Author contributions

Lifang Yin: conceptualization, methodology, validation, formal analysis, investigation, data curation, writing – original draft, visualization. Yi Zhao and Qiang Gao: validation, formal analysis, data curation. Yajun Yin, Tengfei He, and Yufei Yang: methodology. Aimin Ren, Tongshun Wu, and Hui Li: validation, methodology. Luyi Zou: conceptualization, methodology, formal analysis, resources, supervision, project administration, writing – review & editing.

Conflicts of interest

There are no conflicts to declare.

Data availability

Data are available in the supplementary information (SI) and from the authors on request. Supplementary information is available. See DOI: https://doi.org/10.1039/d5sc06741c.

Acknowledgements

References

1 G. Hong, X. Gan, C. Leonhardt, Z. Zhang, J. Seibert, J. M. Busch and S. Bräse, *Adv. Mater.*, 2021, **33**, 2005630.

2 H. Uoyama, K. Goushi, K. Shizu, H. Nomura and C. Adachi, *Nature*, 2012, **492**, 234–238.

3 Y. Olivier, M. Moral, L. Muccioli and J.-C. Sancho-García, *J. Mater. Chem. C*, 2017, **5**, 5718–5729.

4 Y. Olivier, B. Yurash, L. Muccioli, G. D'Avino, O. Mikhnenko, J. C. Sancho-García, C. Adachi, T. Q. Nguyen and D. Beljonne, *Phys. Rev. Mater.*, 2017, **1**, 075602.

5 A. Pershin, D. Hall, V. Lemaur, J.-C. Sancho-Garcia, L. Muccioli, E. Zysman-Colman, D. Beljonne and Y. Olivier, *Nat. Commun.*, 2019, **10**, 597.

6 T. Hatakeyama, K. Shiren, K. Nakajima, S. Nomura, S. Nakatsuka, K. Kinoshita, J. Ni, Y. Ono and T. Ikuta, *Adv. Mater.*, 2016, **28**, 2777–2781.

7 X.-C. Fan, K. Wang, Y.-Z. Shi, Y.-C. Cheng, Y.-T. Lee, J. Yu, X.-K. Chen, C. Adachi and X.-H. Zhang, *Nat. Photonics*, 2023, **17**, 280–285.

8 H. J. Kim and T. Yasuda, *Adv. Opt. Mater.*, 2022, **10**, 2201714.

9 Z. Xue, Y. Hu, S. Xiao, J. Liu, J. Miao and C. Yang, *Angew. Chem., Int. Ed.*, 2025, **64**, e202500108.

10 J.-J. Hu, X. Liang, Z.-P. Yan, J.-Q. Liang, H.-X. Ni, L. Yuan, J.-L. Zuo and Y.-X. Zheng, *Angew. Chem., Int. Ed.*, 2025, **64**, e202421102.

11 Y. Kondo, K. Yoshiura, S. Kitera, H. Nishi, S. Oda, H. Gotoh, Y. Sasada, M. Yanai and T. Hatakeyama, *Nat. Photonics*, 2019, **13**, 678–682.

12 J. Liu, Y. Zhu, T. Tsuboi, C. Deng, W. Lou, D. Wang, T. Liu and Q. Zhang, *Nat. Commun.*, 2022, **13**, 4876.

13 X. Wu, S. Ni, C.-H. Wang, W. Zhu and P.-T. Chou, *Chem. Rev.*, 2025, **125**, 6685–6752.

14 H. Jiang, J. Jin and W.-Y. Wong, *Adv. Funct. Mater.*, 2023, **33**, 2306880.

15 Q.-Y. Meng, R. Wang, Y.-L. Wang, X.-W. Guo, Y.-Q. Liu, X.-L. Wen, C.-Y. Yao and J. Qiao, *Nat. Commun.*, 2023, **14**, 3927.

16 B. H. Jhun, Y. Park, H. S. Kim, J. H. Baek, J. Kim, E. Lee, H. Moon, C. Oh, Y. Jung, S. Choi, M.-H. Baik and Y. You, *Nat. Commun.*, 2025, **16**, 392.

17 X. Huang, J. Liu, Y. Xu, G. Chen, M. Huang, M. Yu, X. Lv, X. Yin, Y. Zou, J. Miao, X. Cao and C. Yang, *Natl. Sci. Rev.*, 2024, **11**, nwae115.

18 Y. X. Hu, J. Miao, T. Hua, Z. Huang, Y. Qi, Y. Zou, Y. Qiu, H. Xia, H. Liu, X. Cao and C. Yang, *Nat. Photonics*, 2022, **16**, 803–810.

19 I. S. Park, H. Min and T. Yasuda, *Angew. Chem., Int. Ed.*, 2022, **61**, e202205684.

20 Y. Li, B. Zhang, A. Ren, D. Wang, J. Zhang, C. Nie, Z. Su and L. Zou, *Chem. Eng. J.*, 2024, **501**, 157676.

21 C. Erker and T. Basché, *J. Am. Chem. Soc.*, 2022, **144**, 14053–14056.

22 Y. Zhang, D. Zhang, T. Huang, A. J. Gillett, Y. Liu, D. Hu, L. Cui, Z. Bin, G. Li, J. Wei and L. Duan, *Angew. Chem., Int. Ed.*, 2021, **60**, 20498–20503.

23 Y. Liu, X. Xiao, Y. Ran, Z. Bin and J. You, *Chem. Sci.*, 2021, **12**, 9408–9412.

24 X. Fan, X. Hao, F. Huang, J. Yu, K. Wang and X. Zhang, *Adv. Sci.*, 2023, **10**, 2303504.

25 H. Hirai, K. Nakajima, S. Nakatsuka, K. Shiren, J. Ni, S. Nomura, T. Ikuta and T. Hatakeyama, *Angew. Chem., Int. Ed.*, 2015, **54**, 13581–13585.

26 E. Runge and E. K. U. Gross, *Phys. Rev. Lett.*, 1984, **52**, 997–1000.

27 L. Y. Zou, Z. L. Zhang, A. M. Ren, X. Q. Ran and J. K. Feng, *Theor. Chem. Acc.*, 2010, **126**, 361–369.

28 T.-F. He, A.-M. Ren, Y.-N. Chen, X.-L. Hao, L. Shen, B.-H. Zhang, T.-S. Wu, H.-X. Zhang and L.-Y. Zou, *Inorg. Chem.*, 2020, **59**, 12039–12053.

29 Y.-L. Zhang, T.-F. He, Z.-K. Zhao, A. Shen, Q. Gao, A.-M. Ren, Z.-M. Su, H. Li, H.-Y. Chu and L.-Y. Zou, *Inorg. Chem.*, 2023, **62**, 7753–7763.

30 M. J. Frisch, G. W. Trucks, H. B. Schlegel, G. E. Scuseria, M. A. Robb, J. R. Cheeseman, G. Scalmani, V. Barone, G. A. Petersson, H. Nakatsuji, X. Li, M. Caricato, A. V. Marenich, J. Bloino, B. G. Janesko, R. Gomperts, B. Mennucci, H. P. Hratchian, J. V. Ortiz, A. F. Izmaylov, J. L. Sonnenberg, D. Williams-Young, F. Ding, F. Lipparini, F. Egidi, J. Goings, B. Peng, A. Petrone, T. Henderson, D. Ranasinghe, V. G. Zakrzewski, J. Gao, N. Rega, G. Zheng, W. Liang, M. Hada, M. Ehara, K. Toyota, R. Fukuda, J. Hasegawa, M. Ishida, T. Nakajima, Y. Honda, O. Kitao, H. Nakai, T. Vreven, K. Throssell, J. A. Montgomery Jr, J. E. Peralta, F. Ogliaro, M. J. Bearpark, J. J. Heyd, E. N. Brothers, K. N. Kudin, V. N. Staroverov, T. A. Keith, R. Kobayashi, J. Normand, K. Raghavachari, A. P. Rendell, J. C. Burant, S. S. Iyengar, J. Tomasi, M. Cossi, J. M. Millam, M. Klene, C. Adamo, R. Cammi, J. W. Ochterski, R. L. Martin, K. Morokuma, O. Farkas, J. B. Foresman and D. J. Fox, *Gaussian 16 Rev. C.01*, Wallingford, CT, 2016.

31 P. J. Stephens, F. J. Devlin, C. F. Chabalowski and M. J. Frisch, *J. Phys. Chem.*, 1994, **98**, 11623–11627.

32 S. Grimme, J. Antony, S. Ehrlich and H. Krieg, *J. Chem. Phys.*, 2010, **132**, 154104.

33 S. Grimme, S. Ehrlich and L. Goerigk, *J. Comput. Chem.*, 2011, **32**, 1456–1465.

34 D. Andrae, U. Häußermann, M. Dolg, H. Stoll and H. Preuß, *Theor. Chim. Acta*, 1990, **77**, 123–141.

35 P. C. Hariharan and J. A. Pople, *Mol. Phys.*, 1974, **27**, 209–214.

36 O. Christiansen, H. Koch and P. Jørgensen, *Chem. Phys. Lett.*, 1995, **243**, 409–418.

37 A. Hellweg, S. A. Grün and C. Hättig, *Phys. Chem. Chem. Phys.*, 2008, **10**, 4119–4127.

38 D. Hall, J. C. Sancho-García, A. Pershin, G. Ricci, D. Beljonne, E. Zysman-Colman and Y. Olivier, *J. Chem. Theory Comput.*, 2022, **18**, 4903–4918.

39 D. Mester, P. R. Nagy, J. Csóka, L. Gyevi-Nagy, P. B. Szabó, R. A. Horváth, K. Petrov, B. Hégely, B. Ladóczki, G. Samu, B. D. Lőrincz and M. Kállay, *J. Phys. Chem. A*, 2025, **129**, 2086–2107.

40 Mrcc, a quantum chemical program suite written by M. Kállay, P. R. Nagy, D. Mester, L. Gyevi-Nagy, J. Csóka, P. B. Szabó, Z. Rolik, G. Samu, B. Hégely, B. Ladóczki, K. Petrov, J. Csontos, Á. Ganyecz, I. Ladjánszki, L. Szegedy, M. Farkas, P. D. Mezei, R. A. Horváth, and B. D. Lőrincz, See https://www.mrcc.hu/.

41 F. Neese, *Wiley Interdiscip. Rev.: Comput. Mol. Sci.*, 2022, **12**, e1606.

42 E. van Lenthe, A. Ehlers and E.-J. Baerends, *J. Chem. Phys.*, 1999, **110**, 8943–8953.

43 E. van Lenthe, J. G. Snijders and E. J. Baerends, *J. Chem. Phys.*, 1996, **105**, 6505–6516.

44 F. Weigend and R. Ahlrichs, *Phys. Chem. Chem. Phys.*, 2005, **7**, 3297–3305.

45 Y. Niu, L. Wenqiang, P. Qian, G. Hua, Y. Yuanping, W. Linjun, N. Guangjun, W. Dong and Z. Shuai, *Mol. Phys.*, 2018, **116**, 1078–1090.

46 Z.-K. Zhao, T.-F. He, Q. Gao, A.-M. Ren, T.-S. Wu, J.-F. Guo, H.-Y. Chu, Z.-M. Su, H. Li and L.-Y. Zou, *Inorg. Chem.*, 2024, **63**, 17435–17448.

47 B. de Souza, F. Neese and R. Izsák, *J. Chem. Phys.*, 2018, **148**, 034104.

48 K. Shizu and H. Kaji, *Nat. Commun.*, 2024, **15**, 4723.

49 K. Shizu and H. Kaji, *J. Phys. Chem. A*, 2021, **125**, 9000–9010.

50 Q. Peng, Y. Yi, Z. Shuai and J. Shao, *J. Am. Chem. Soc.*, 2007, **129**, 9333–9339.

51 Q. Peng, D. Fan, R. Duan, Y. Yi, Y. Niu, D. Wang and Z. Shuai, *J. Phys. Chem. C*, 2017, **121**, 13448–13456.

52 X. Zou, N. Gan, Z. Lin, H. Ma, Y. Wu, A. Lv, Z. An, L. Gu and W. Huang, *Nat. Commun.*, 2025, **16**, 6412.

53 L. Ge, W. Zhang, Y.-H. Hao, M. Li, Y. Liu, M. Zhou and L.-S. Cui, *J. Am. Chem. Soc.*, 2024, **146**, 32826–32836.

54 R. J. Gillespie, *J. Chem. Educ.*, 1963, **40**, 295.

55 T. Lu and F. Chen, *J. Comput. Chem.*, 2012, **33**, 580–592.

56 R. C. Hilborn, *Am. J. Phys.*, 1982, **50**, 982–986.

57 X.-K. Chen, Y. Tsuchiya, Y. Ishikawa, C. Zhong, C. Adachi and J.-L. Brédas, *Adv. Mater.*, 2017, **29**, 1702767.

58 X.-K. Chen, D. Kim and J.-L. Brédas, *Acc. Chem. Res.*, 2018, **51**, 2215–2224.

59 T. He, W. Zhao, M. Lin, B. Sun, Y. Chen, H.-L. Zhang and G. Long, *J. Phys. Chem. Lett.*, 2024, **15**, 9844–9851.

60 P. O. Andersson, S. M. Bachilo, R.-L. Chen and T. Gillbro, *J. Phys. Chem.*, 1995, **99**, 16199–16209.

61 J. Zhao, H. Liu, J. Fan and Q. Mu, *Phys. Chem. Chem. Phys.*, 2024, **26**, 5156–5168.

62 Y. Pu, X. Cai, Y. Qu, W. Cui, L. Li, C. Li, Y. Zhang and Y. Wang, *Angew. Chem., Int. Ed.*, 2025, **64**, e202420253.

63 X. Cai, Y. Pan, C. Li, L. Li, Y. Pu, Y. Wu and Y. Wang, *Angew. Chem., Int. Ed.*, 2024, **63**, e202408522.

64 A. Ying, N. Li, X. Chen, J. Xia, C. Yang and S. Gong, *Chem. Sci.*, 2025, **16**, 784–792.

65 A. Ying, L. Zhan, Y. Tan, X. Cao, C. Yang and S. Gong, *Sci. China: Chem.*, 2023, **66**, 2274–2282.

66 S. Diesing, L. Zhang, E. Zysman-Colman and I. D. W. Samuel, *Nature*, 2024, **627**, 747–753.

67 M. Elsherbini, W. S. Hamama and H. H. Zoorob, *Coord. Chem. Rev.*, 2017, **330**, 110–126.